Abdolali, Ali, Kadri, Usama , Parsons, Wade and Kirby, James T. 2018. On the propagation of acoustic-gravity waves under elastic ice sheets. Journal of Fluid Mechanics 837 , pp. 640-656. 10.1017/jfm.2017.808

Publishers page: http://dx.doi.org/10.1017/jfm.2017.808

On the propagation of acoustic-gravity waves under elastic ice sheets

Journal:	*Journal of Fluid Mechanics*
Manuscript ID	JFM-17-S-0635.R1
mss type:	Standard
Date Submitted by the Author:	25-Sep-2017
Complete List of Authors:	Abdolali, Ali; National Oceanic and Atmospheric Administration, NWS/NCEP/Environmental Modeling Center; University Corporation for Atmospheric Research Kadri, Usama; Massachusetts Institute of Technology, Mechanical Engineering; Cardiff University, School of Mathematics Parsons, Wade; Memorial University of Newfoundland, Faculty of Engineering and Applied Science Kirby, James; University of Delaware, Center for Applied Coastal Research
Keyword:	Compressible Flows, Geophysical and Geological Flows, Waves/Free-surface Flows

On the propagation of acoustic–gravity waves under elastic ice sheets

Ali Abdolali[1,2] †, **Usama Kadri**[3,4], **Wade Parsons**[5], **James T. Kirby**[6]

[1]NWS/NCEP/Environmental Modeling Center, National Oceanic and Atmospheric Administration (NOAA), College Park MD 20740 USA

[2] University Corporation for Atmospheric Research (UCAR), Boulder, CO 80301 USA

[3] School of Mathematics, Cardiff University, Cardiff, CF24 4AG, UK

[4] Department of Mathematics, Massachusetts Institute of Technology, Cambridge, MA 02139, USA

[5] Faculty of Engineering and Applied Science, Memorial University of Newfoundland 240 Prince Phillip Drive, St. John's, NL A1B 3X5 Canada

[6]Center for Applied Coastal Research, Department of Civil and Environmental Engineering, University of Delaware, Newark DE 19716 USA

(Received xx; revised xx; accepted xx)

The propagation of wave disturbances in water of varying depth bounded above by ice sheets is discussed, accounting for gravity, compressibility and elasticity effects. Considering the more realistic scenario of elastic ice sheets reveals a continuous spectrum of acoustic–gravity modes that propagate even below the cut-off frequency of the rigid surface solution where surface (gravity) waves cannot exist. The balance between gravitational forces and oscillations in the ice sheet defines a new dimensionless quantity $\mathcal{K}a$. When the ice sheet is relatively thin and the prescribed frequency is relatively low ($\mathcal{K}a \ll 1$), the free-surface bottom pressure solution is retrieved in full. However, thicker ice sheets or propagation of relatively higher frequency modes ($\mathcal{K}a \gg 1$) alter the solution fundamentally, which is reflected in amplified asymmetric signature and different characteristics of the eigenvalues, such that the bottom pressure is amplified when acoustic–gravity waves are transmitted to shallower waters. To analyze these scenarios, an analytical solution and a depth-integrated equation are derived for the cases of constant and varying depths, respectively. Together, these are capable to model realistic ocean geometries and inhomogeneous distribution of ice sheets.

Key words: acoustic–gravity waves, elasticity, waves/ice interaction

1. Introduction

The propagation of wave disturbances accounting for both gravity and compressibility effects has been increasingly attracting attention for studying acoustic–gravity wave (AGW) theory, due to the broad applications of high societal and scientific impact. To name a few, AGW theory has been employed in the context of tsunami early detection (Yamamoto 1982; Stiassnie 2010; Kadri & Stiassnie 2012; Cecioni *et al.* 2014; Oliveira & Kadri 2016; Kadri 2017); volcanic eruptions and storms (Caplan-Auerbach *et al.* 2014; Renzi & Dias 2014); nonlinear interaction and energy exchange with the upper ocean

---

† Email address for correspondence: ali.abdolali@noaa.gov

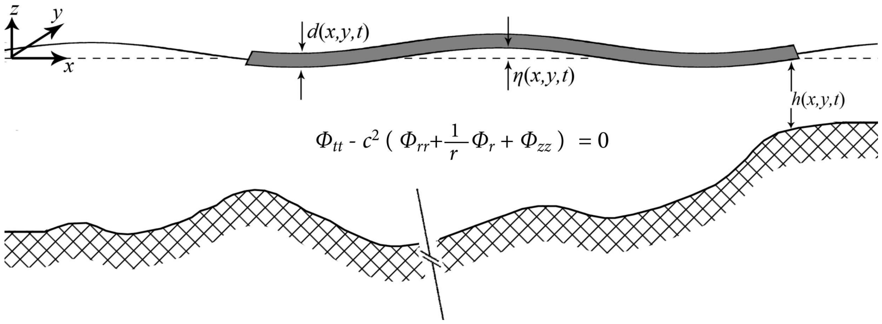

FIGURE 1. Schematic view of fluid domain

(Kadri & Stiassnie 2013; Kadri 2015, 2016*b*; Kadri & Akylas 2016); deep ocean water transport (Kadri 2014); and the effect of earth–sea system coupling which has lead to a better understanding of propagation of wave disturbances at the interface of two media (Chierici *et al.* 2010; Eyov *et al.* 2013; Abdolali *et al.* 2015; Kadri 2016*a*).

Due to the increasing effects of climate change and sea level rise, a climb in the frequency and destructiveness of natural disasters in arctic zones is foreseen (Hansen 2007). These include, but are not limited to, submarine earthquakes and mass failure and oscillation of large ice blocks. The latter can be possibly triggered by storms, atmospheric and ocean currents, ice block shrinkage, ice slide and ice-quakes. To tackle this problem, a proper surface boundary condition is thus required. The vast majority of literature on the propagation of wave disturbances in a compressible ocean under the effects of gravity considers the upper boundary as a free-surface leading to the mutual generation of surface-gravity waves and AGWs. In the presence of a layer of ice on the surface the properties of the aforementioned waves may change fundamentally. Recently, Kadri (2016*a*) studied the generation of AGWs by a vertically oscillating rigid ice block, and argued that at the given settings, and without elasticity, gravity waves cannot be accounted for, and acoustic modes propagate at very specific frequencies.

In the present paper, we examine the effects of elasticity focusing on AGWs in a water column of depth $h(x; y; t)$ bounded by a rigid bottom, and allowing either a free-surface or an elastic ice sheet at the surface of thickness $d(x, y, t)$. The vertical coordinate, z, is measured positively upwards from the undisturbed surface, and x and y denote the horizontal Cartesian coordinates as illustrated in Fig. 1. The presence of an ice layer often requires deriving proper orthogonality relations (Zakharov 2008). Nevertheless, note that here the acoustic–gravity lengthscale far exceeds the width of the ice layer which is confined to the surface, and thus all energy initially found in the AGWs will effectively remain in the liquid layer. Therefore, transmission to or reflection from the ice layer is neglected. The governing equations are described in a velocity potential form and applied to a circular disturbance (§2). The role of an elastic ice sheet on the surface compared to free surface and rigid ice sheet is investigated in §3. An analytical closed form solution of the bottom pressure is derived, and computations are carried out for the case of constant depth (§4). Then, in order emphasize the role of the ice sheets we consider variable ice thickness, water depth and source, and a depth-integrated mild-slope equation is developed and validated (§5 and §6). Finally, concluding remarks are given in §7.

2. Governing equations

For a circular disturbance of radius R, the governing equation in cylindrical form ($x^2 + y^2 = r^2$) for linearised, inviscid motion in a compressible medium with velocity determined by the gradient of a potential, $\mathbf{u} = \nabla \Phi$ is given by

$$\Phi_{tt} - c^2 \left(\Phi_{rr} + \frac{1}{r}\Phi_r + \Phi_{zz} \right) = 0; \qquad -h \leqslant z \leqslant 0, \tag{2.1}$$

where c is the sound speed in water. The bottom boundary condition is given by

$$\Phi_z + h_t + \Phi_r \cdot h_r = 0; \qquad z = -h, \tag{2.2}$$

$$h_t = -\frac{\zeta_0}{\tau}\mathcal{H}\left(R^2 - r^2\right)\mathcal{H}\left(t(\tau - t)\right), \tag{2.3}$$

where $\mathcal{H}$ is the Heaviside step function, ζ_0 is its final vertical displacement, and τ is the duration of its displacement. The kinematic and dynamic boundary conditions at the free surface, with an overlying ice sheet layer, are

$$\begin{cases} \eta_t = \Phi_z; \\ g\eta + \Phi_t + \frac{\delta P}{\rho} = 0; \end{cases} \qquad z = 0, \tag{2.4}$$

where g is gravitational acceleration, ρ is density of water and δP is the pressure exerted by the moving ice sheet on the water column. Note that (2.1) neglects the background compressibility of the static water column. This effect is important for the long range propagation of tsunamis, for example, but has been shown to be negligible for the acoustic modes of propagation; see Abdolali & Kirby (2017). The equation for pressure exerted by an elastic ice sheet on the underlying water column is given by Schulkes *et al.* (1987),

$$\delta P = \rho_i d \eta_{tt} + D\nabla_r^4 \eta + T\nabla_r^2 \eta, \tag{2.5}$$

which includes the effect of the weight of the ice layer relative to its vertical motion, the effect of bending stress, and the effect of in-plane tension or compression in the ice layer ($T > 0$ corresponds to compression). Note that the lateral stress T has to be effectively large to impact wave propagation, therefore $T = 0$ is taken in this study. Here we consider an ice sheet of density $\rho_i = 917$ kg/m^3, thickness d, Young's elastic modulus $E = 10^9$N m^{-2} and Poisson's ratio $\nu = 1/3$. The flexural rigidity of ice is defined by Hosking *et al.* (1988),

$$D = \frac{d^3 E}{12(1-\nu^2)} = c_i^2 \rho_i \frac{d^3}{12}, \tag{2.6}$$

where $c_i = 3700$ m/s is the sound speed in the ice layer. Combining the dynamic and kinematic boundary conditions at the surface equations (2.4) and (2.5) yields

$$\rho g \Phi_z + \rho \Phi_{tt} + \rho_i d \Phi_{ttz} + D\nabla_r^2(\nabla_r^2 \Phi_z) + T\nabla_r^2 \Phi_z = 0; \qquad z = 0. \tag{2.7}$$

3. The Role of the Ice Sheet

A calculation was carried out for the case of constant depth for different flexible ice sheet thickness on the surface compared to free surface ($d = 0$). The governing equation in fluid and boundary conditions at the surface and bottom are defined in Eqs. (2.1), (2.2), and (2.4). We used $h = 1500$ m, $\rho = 1024$ kg/m^3, $\rho_i = 917$ kg/m^3, $c = 1500$ m/s, $c_i = 3700$ m/s, for a unit source area with semi-length $b = 15$ km and $h_t = \sin(2\pi f_0 t)$ for rise time $\tau = 2/f_0 = 5$ s. The results are depicted in Fig. 2 for the case of ice sheet

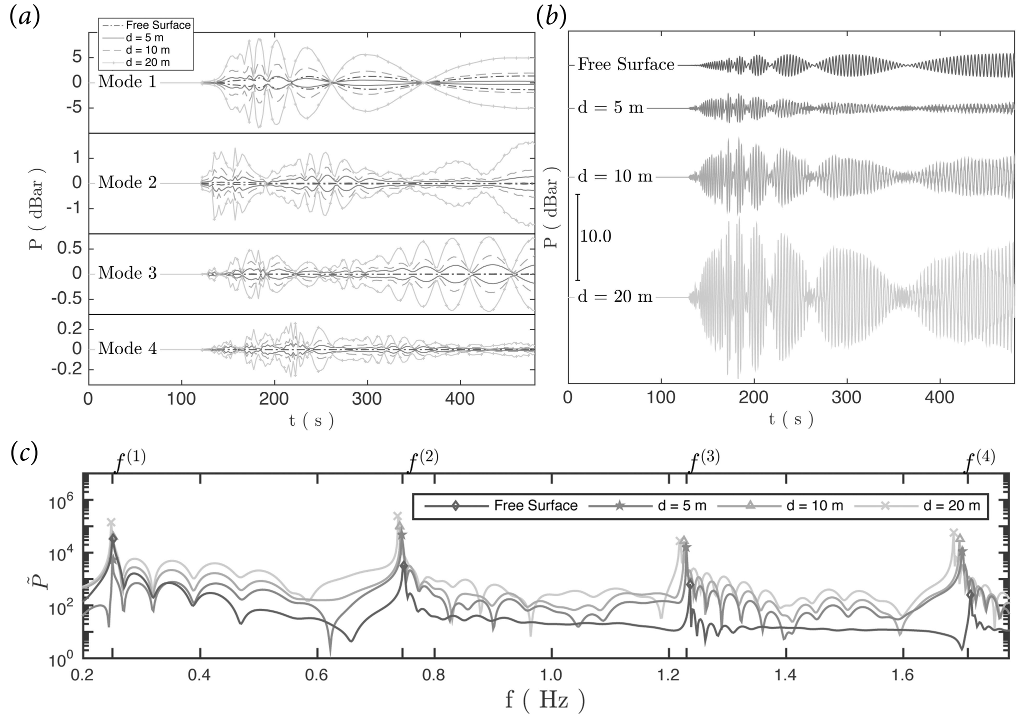

FIGURE 2. The pressure time series and corresponding spectrum plotted 200 km from the epicentre at $z = 0$ with different ice thickness, $d = 0$ (free surface), 5, 10 and 20 m, in a constant depth $h = 1500$ m, for a unit source area with semi-length $b = 15$ km and $h_t = \sin(2\pi f_0 t)$ for rising time $\tau = 2/f_0 = 5$ s. Panel (a): Envelope for the first 4 modes for different ice thickness. The comparison in each subplot is for different ice thickness comparing the amplitude of a given mode for different ice thickness. Panel (b): Superposition of acoustic modes. Panel (c): Frequency spectrum for whole time series.

thickness $d = 0$ (black) and $d = 5,\ 10$ and 20 m at 200 km from the epicentre. Panel (a) shows the envelope of pressure time series for four first modes; panel (b) shows the superposition of acoustic modes P; and panel (c) shows the corresponding frequency spectrum $\tilde{P}$. For the case of free surface boundary condition (d=0), the majority of energy is in the first mode. Increasing the ice thickness amplifies the pressure below the surface and also manifests in higher modes (unlike the case of the free surface).

The frequency spectrum of pressure signals at $z = 0$ calculated from a sets of computations, for the case of free surface, rigid and flexible ice sheets on the surface are shown in Fig. 3. The water depth is $h = 3000$ m, semi-fault length $b = 30$ km and $h_t = \sin(2\pi f_0 t)$ for $f_0 = 0.55$ Hz. For the case of rigid bottom, the peak frequencies are calculated by $f^{(n)} = nc/2h$ whereas for the case of free surface and flexible ice sheet, it can be evaluated by $f^{(n)} = (2n-1)c/4h$, where $\omega = 2\pi f$.

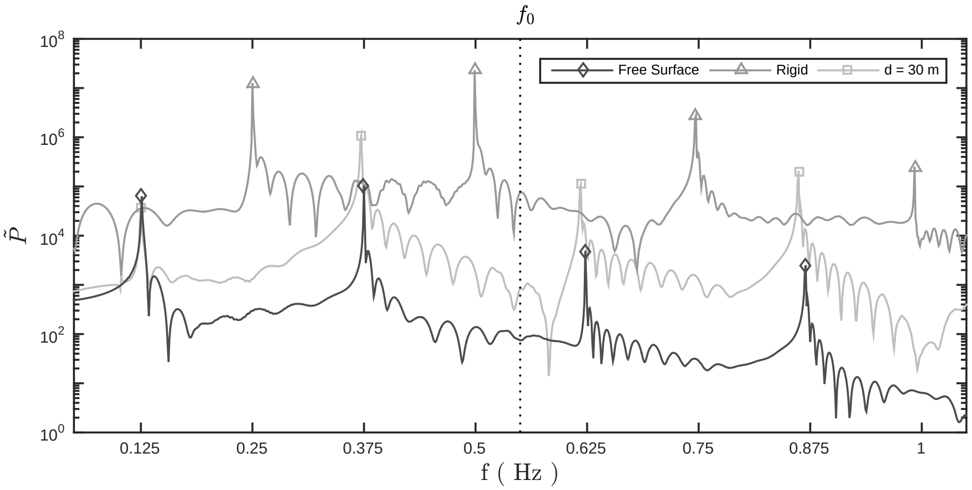

FIGURE 3. Pressure spectrum at $z = 0$ for the case of free surface, rigid and flexible ice sheet ($d = 30$ m), in a constant depth $h = 3000$ m, for a unit source area with semi-length $b = 30$ km and $h_t = \sin(2\pi f_0 t)$ for $f_0 = 0.55$ Hz shown by vertical dotted line and rising time $\tau = 2/f_0$. The peak frequencies for the case of rigid ice sheet on the surface can be evaluated by $f^{(n)} = nc/2h = 0.25,\ 0.5,\ 0.75,\ 1,\ ...$ Hz while for the case of free surface and flexible ice sheet can be approximated by $f^{(n)} = (2n-1)c/4h = 0.125,\ 0.375,\ 0.625,\ 0.825,\ ...$ Hz .

4. Analytical solution

4.1. *Dispersion relation*

Defining the Fourier transform of the velocity potential

$$\varphi(r, z, \omega) = \frac{1}{\sqrt{2\pi}} \int_{-\infty}^{\infty} \Phi(r, z, t) \exp(-\mathrm{i}\omega t)\mathrm{d}t, \tag{4.1}$$

the governing equation and boundary conditions become

$$\frac{\omega^2}{c^2}\varphi + \nabla_r^2\varphi + \varphi_{zz} = 0; \qquad -h \leqslant z \leqslant 0, \tag{4.2}$$

$$-\omega^2\varphi + \left(g - \tilde{\rho} d\omega^2\right) + \tilde{D}\nabla_r^2\left(\nabla_r^2\varphi_z\right) + \tilde{T}\nabla_r^2\varphi_z = 0; \qquad z = 0, \tag{4.3}$$

$$\varphi_z + \frac{\mathrm{i}\zeta_0}{\tau\sqrt{2\pi}} \frac{1 - \mathrm{e}^{-\mathrm{i}\omega\tau}}{\omega} \mathcal{H}\left(R^2 - r^2\right); \qquad z = -h, \tag{4.4}$$

where ∇_r^2 is the horizontal gradient, $\tilde{\rho} = \rho_i/\rho$, $\tilde{D} = D/\rho g$, $\tilde{T} = T/\rho g$. Using the method of separation of variables the field equation results in two ordinary differential equations, which upon substitution in the boundary conditions result in the dispersion relation,

$$\omega^2 = -\frac{g\lambda_n \tan(\lambda_n h)}{1 - \tilde{d}\lambda_n \tan(\lambda_n h)} \left(1 + \tilde{D}k_n^4 - \tilde{T}k_n^2\right), \tag{4.5}$$

where $\tilde{d} = \tilde{\rho} d$, subscript n denotes the mode number, and

$$\lambda_n^2 = \frac{\omega^2}{c^2} - k_n^2. \tag{4.6}$$

For AGWs λ_n and k_n are real, and $n = 1, 2, ..., N$ where N is the highest possible

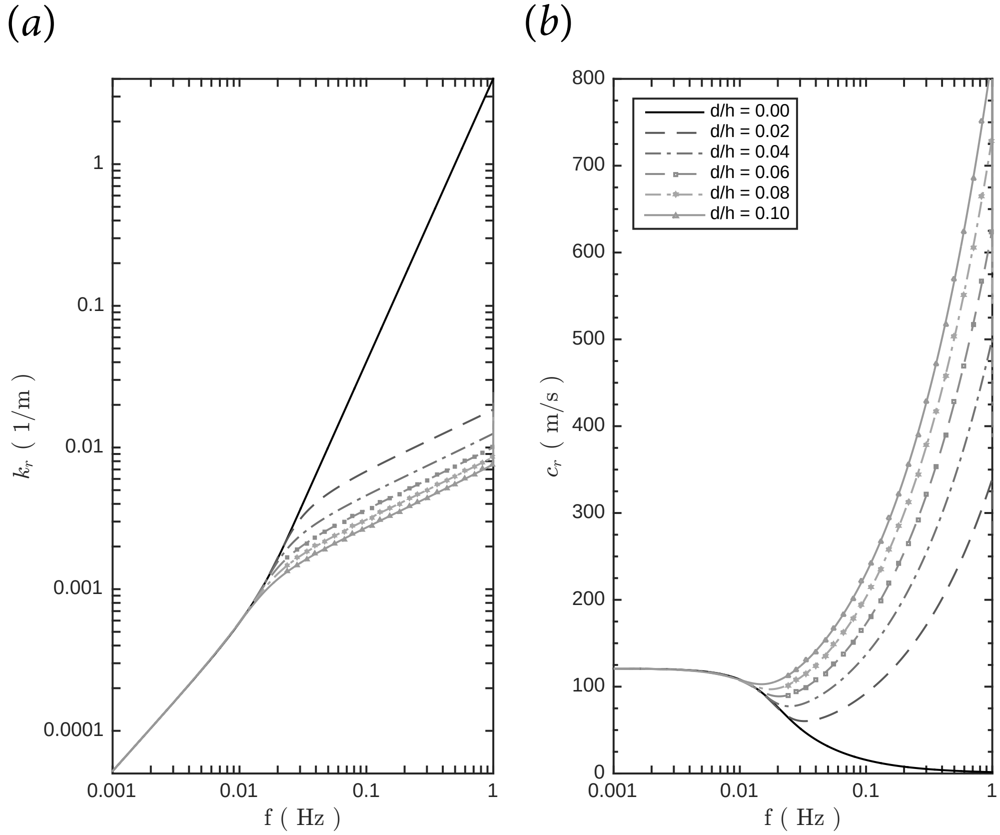

FIGURE 4. Gravity wave number $k_r^2 = \omega^2/c^2 + \lambda_0^2$ for imaginary roots of the dispersion relation λ_0 Eq. (4.5) for varying ice sheet thickness d/h (panel *a*); Phase celerity c_r (panel *b*). The solid black line is for the case of free surface.

AGW number; for the surface-gravity mode λ_0 is imaginary and k_0 is real; and for the evanescent modes k_n is imaginary, with $n > N$. When there is no overlying ice sheet, $d = 0$, (4.5) reduces to the classical dispersion relation given by $\omega^2 = -g\lambda_n \tan(\lambda_n h)$. In Fig. 4, gravity wave number k_r and phase celerity $c_r = \omega/k_r$ are shown in panel (*a*) and (*b*) respectively for varying ice sheet thickness $0 \leqslant d/h \leqslant 0.1$ where $h = 1500$ m. Comparison between wave numbers in the presence of ice sheet and for the case of free surface $d = 0$ shows that for lower frequencies, the gravity wave numbers are identical and at higher frequencies, the wave number is reduced with respect to free surface condition. It shows that inclusion of the elastic ice sheet in the dispersion relation is negligible for long period waves like tsunamis, tides and surges, while, for shorter waves, this effect is significant. On the other hand and in Fig. 5, the solutions of dispersion relation for real separation variables λ_n are shown for the first three acoustic modes. For a given frequency, if $k_n^2 = \omega^2/c^2 - \lambda_n^2 \leqslant 0$, the acoustic mode is evanescent whereas for $k_n^2 > 0$, the acoustic mode is progressive. In order to compare the separation variable changes due to presence or absence of ice sheet on the surface, λ_n are plotted for $0 \leqslant d/h \leqslant 0.1$ in panel (*a*). The corresponding phase celerity compared to $d = 0$ case is shown in panel (*b*).

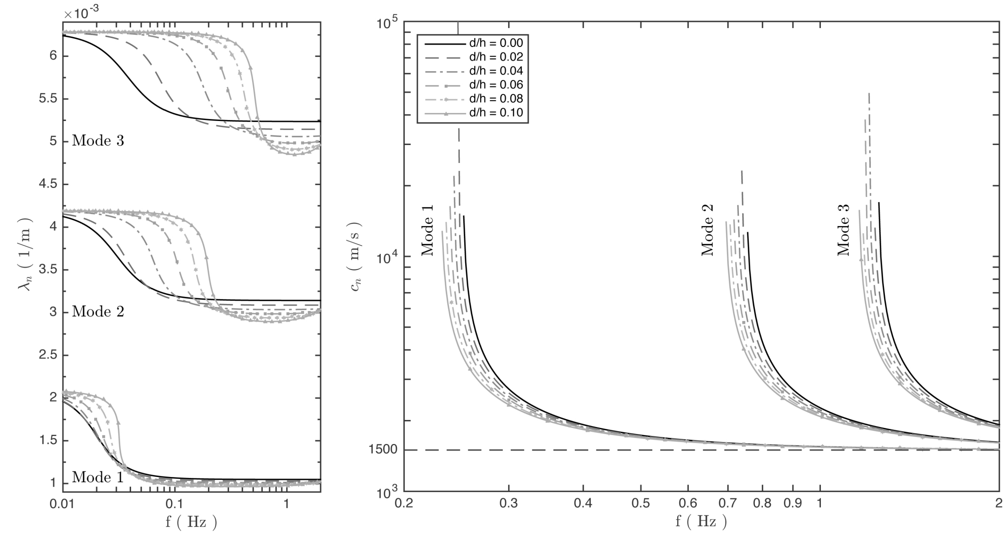

FIGURE 5. Dispersion relation solution for acoustic gravity modes ($\lambda_{n=1,2,3}$) obtained from Eq. (4.5) for varying ice sheet thickness d/h (panel *a*); The corresponding phase celerity (panel *b*). The frequency range where $k_n^2 = \omega^2/c^2 + \lambda_n^2 \leqslant 0$, represent evanescent mode where mode n is not propagating. The solid black line is for the case of free surface.

Rearranging eq.(4.5) by isolating $\tan(\lambda_n h)$ leads to the form

$$\tan(\lambda_n h) = \frac{1}{\lambda_n \tilde{d}\,(1-\mathcal{K}a)\left(1+\tilde{D}k_n^4-\tilde{T}k_n^2\right)}, \tag{4.7}$$

where $\mathcal{K}a \equiv g/\tilde{d}\omega^2$ is a dimensionless quantity that accounts for the effects of gravity relative to oscillations in the ice sheet layer. This quantity can also be described by $\mathcal{K}a = \mathrm{Fr}^{-1}\mathrm{St}^{-2}$, where Fr and St present the Froude and Strouhal numbers. For the leading AGWs corresponding $k_n \ll 1$, the term $(\tilde{D}k_n^4 - \tilde{T}k_n^2)$ can be neglected, and the contribution of the ice sheet is encapsulated in the thickness of the ice sheet, or equivalently by $\mathcal{K}a$. The eigenvalues change fundamentally depending on whether $\mathcal{K}a \gg 1$ or $\mathcal{K}a \ll 1$, and can be approximated by

$$\lambda_n h = \begin{cases} \left(n-\frac{1}{2}\right)\pi, & \mathcal{K}a \gg 1, \\ (n-1)\pi, & \mathcal{K}a \ll 1. \end{cases} \tag{4.8}$$

This unique characteristics for the propagation of AGWs under elastic ice sheets is illustrated in the graphical solution of (4.7) presented in Fig. 6. Note that for the physical AGW problem at hand, the prescribed frequency is $O(1)$ or more; for frequencies much smaller than unity the eigenvalues can be approximated by the rigid solution, though this scenario is not considered here as it is not physical.

In Fig. 7 (panel *a*), gravity k_0 and first four acoustic wave numbers k_n are shown for ice sheet thickness $d = 20$ m, $h = 4000$ m. For a given frequency, the wave number can be either evanescent if $k^2 = \omega^2/c^2 - \lambda^2 \leqslant 0$ or progressive if $k^2 > 0$.

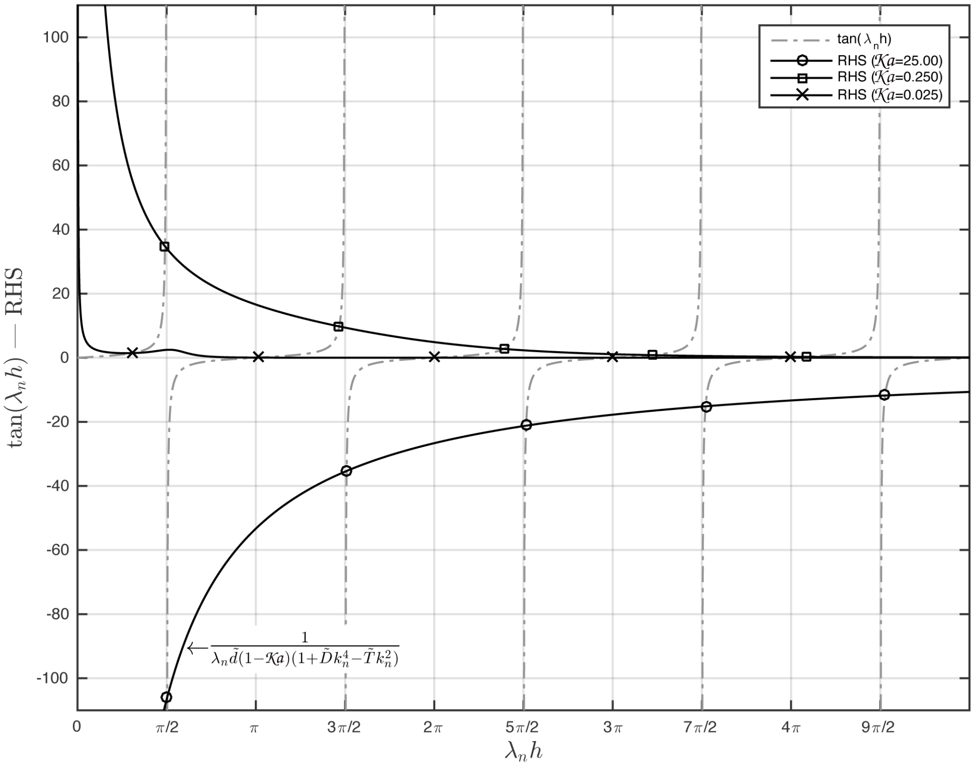

FIGURE 6. Dispersion relation for $\omega = 2\pi/10$ at depth $h = 4000$ m with $\mathcal{K}a = 25,\ 0.25$ and 0.025. The dash-dot lines and solid lines represent the $\tan(\lambda_n h)$ and right hand side (RHS) of (4.7) respectively. The solution of Eq. (4.7) at cross points are shown for each ice thickness. Asymmetric signature can be seen at higher modes when $\mathcal{K}a \ll 1$.

4.2. *Farfield bottom pressure*

The velocity potential is found by constructing inner ($r < R$) and outer ($r > R$) regions, following similar steps as presented by Hendin & Stiassnie (2013). For the inner region one needs to include a particular solution,

$$s(z) = \frac{\mathrm{i}\zeta_0 c}{\tau\sqrt{2\pi}} \frac{1-\mathrm{e}^{-\mathrm{i}\omega\tau}}{\omega^2} \frac{\alpha\cos\left(\dfrac{\omega}{c}z\right)+\sin\left(\dfrac{\omega}{c}z\right)}{\cos\left(\dfrac{\omega}{c}h\right)+\alpha\sin\left(\dfrac{\omega}{c}h\right)}; \qquad \alpha = \frac{g-\tilde{d}\omega^2+\tilde{D}k^4}{\omega\, c}. \tag{4.9}$$

In the inner region the effect of the overlying ice sheet on the propagating modes is amplified. For a free surface, α reduces to $g/\omega c$ and the solution originally obtained by Hendin & Stiassnie (2013) for a circular disturbance at the sea-floor with a free surface condition is retrieved. Following a standard matching technique between the inner and outer regions, and applying continuity at $r = R$, we obtain a solution for AGW modes in the outer region of the form

$$\begin{aligned}\varPhi^{(\mathrm{out})}(r,z,t) = -\frac{4R\zeta_0}{\tau}\sum_{n=1}^{N}\int_{\omega_{sn}}^{\infty}\frac{\lambda_n}{\omega k_n}\frac{\cos\lambda_n(z+h)\sin(\omega\tau/2)}{\sin(2\lambda_n h)+2\lambda_n h} \\ \times J_1(k_nR)\Big[J_0(k_nr)\sin\Big(\omega t-\frac{\omega\tau}{2}\Big)-Y_0(k_nr)\cos\Big(\omega t-\frac{\omega\tau}{2}\Big)\Big]\mathrm{d}\omega,\end{aligned} \tag{4.10}$$

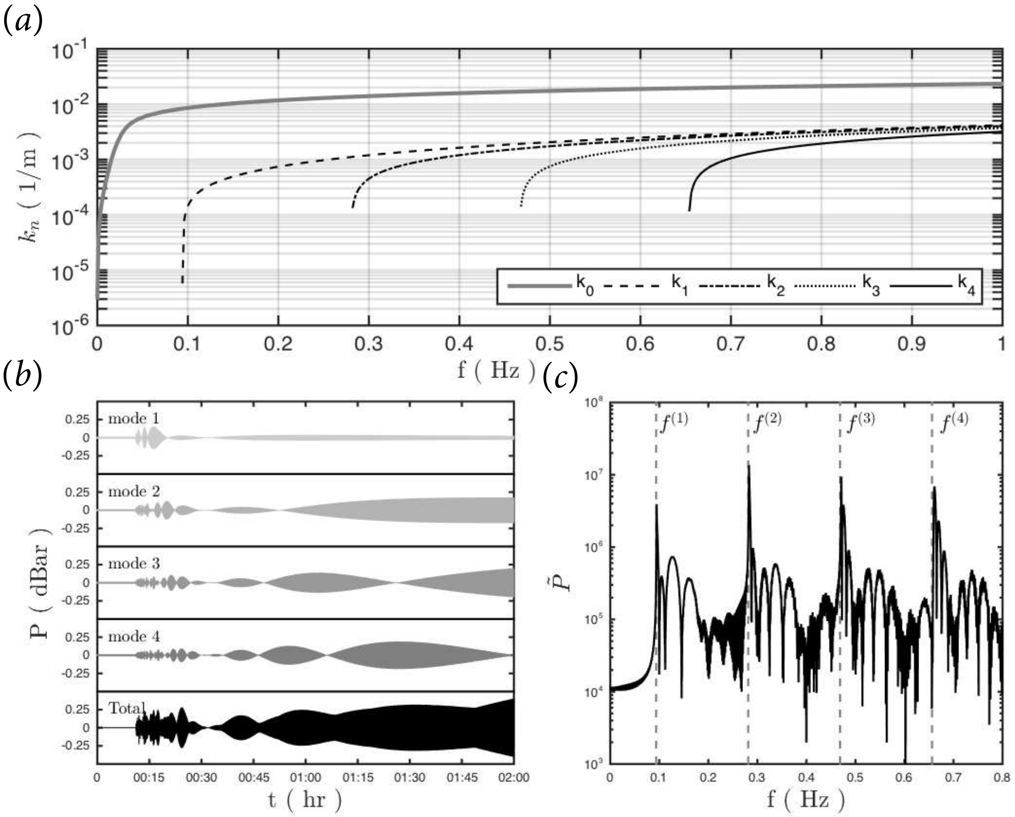

FIGURE 7. Farfield bottom pressure record for the first four AGW modes evaluated by analytical solution (Eq. 4.19) at 1000 km from epicentre for disturbance radius $R = 15$ km, depth $h = 4$ km, duration $\tau = 10$ s and vertical amplitude $\zeta_0 = 1$ m. Panel (a) Gravity wave number and first four imaginary roots of the dispersion relation given by $k_n^2 = \omega^2/c^2 - \lambda_n^2$. Time series of first four AGW modes (panel b) and corresponding spectrum (panel c).

where J and Y are Bessel functions of the first and second kinds. Finally, the bottom pressure is given by $p_b = -\rho\Phi_t$; substituting into (4.10) yields the far-field bottom pressure

$$p_b^{(\text{out})} = \frac{4\rho R\zeta_0}{\tau}\sum_{n=1}^{N}\int_{\omega_{sn}}^{\infty}\frac{\lambda_n}{k_n}\frac{\sin(\omega\tau/2)}{\sin(2\lambda_n h)+2\lambda_n h}J_1(k_n R)$$
$$\times\left[J_0(k_n r)\cos\left(\omega t-\frac{\omega\tau}{2}\right)+Y_0(k_n r)\sin\left(\omega t-\frac{\omega\tau}{2}\right)\right]\mathrm{d}\omega. \tag{4.11}$$

In the far-field, when r is very large, Bessel functions can be approximated asymptotically:

$$J_0(k_n r) = \sqrt{\frac{2}{\pi k_n r}}\cos\left(k_n r-\frac{\pi}{4}\right) \tag{4.12}$$

$$Y_0(k_n r) = \sqrt{\frac{2}{\pi k_n r}}\sin\left(k_n r-\frac{\pi}{4}\right) \tag{4.13}$$

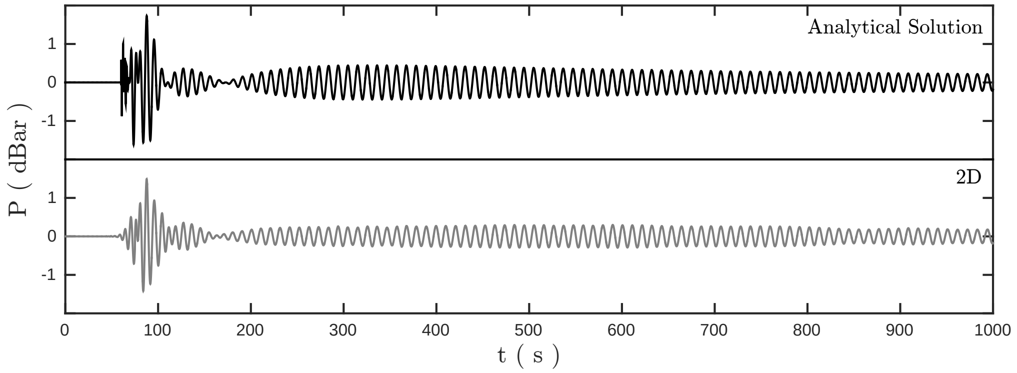

FIGURE 8. Bottom-pressure oscillations of the 1^{st} mode of Acoustic-Gravity wave at 90 km from the epicentre of a circular disturbance according to analytical solution (Eq. 4.19) (black) and depth-integrated model (Eq. 5.4) (grey). The fault and water geometries are similar to Fig. 7.

Substituting the Bessel approximations back into the pressure relation gives

$$p_b^{(\mathrm{out})} = \frac{4\rho R\zeta_0}{\tau}\sum_{n=1}^{N}\int_{\omega_{sn}}^{\infty}\sqrt{\frac{2}{\pi k_n r}}\frac{\lambda_n}{k_n}\frac{\sin(\omega\tau/2)}{\sin(2\lambda_n h)+2\lambda_n h}J_1(k_n R) \times \cos\left(k_n r - \omega t + \frac{\omega\tau}{2} - \frac{\pi}{4}\right)\mathrm{d}\omega. \tag{4.14}$$

Defining the phase of the n-mode as

$$g_n(\omega) = k_n(\omega)\frac{r}{t} - \omega\left(1 - \frac{\tau}{2t}\right) - \frac{\pi}{4t} \quad \text{where} \quad k_n(\omega) = \sqrt{\frac{\omega^2}{c^2} - \lambda_n^2} \tag{4.15}$$

the point of stationary phase is then at $\omega = \omega_{s,n}$ where $\partial g_n/\partial\omega = 0$, so that

$$\frac{\partial g_n}{\partial \omega} = \frac{\omega_{s,n}}{\sqrt{\omega_{s,n}^2/c^2 - \lambda_n^2}}\frac{r}{c^2 t} - \left(1 - \frac{\tau}{2t}\right) = 0 \tag{4.16}$$

or by isolating $\omega_{s,n}$:

$$\omega_{s,n} = \frac{\lambda_{s,n} c}{\sqrt{1 - \left[r/c\,(t-\tau/2)\right]^2}}; \quad k_{s,n} = \frac{\lambda_{s,n}}{\sqrt{\left[r/c\,(t-\tau/2)\right]^2 - 1}} \tag{4.17}$$

where $\lambda_{s,n}$ obeys (4.8) and

$$\frac{\partial^2 g_n}{\partial^2 \omega} = \frac{\lambda_{s,n}^2 r/c^2 t}{\left(\omega_{s,n}^2/c^2 - \lambda_{s,n}^2\right)^{3/2}}. \tag{4.18}$$

So finally we can write,

$$p_b = \frac{8\rho R\zeta_0 c}{r\tau}\sum_{n=1}^{N}\frac{\lambda_{s,n}}{k_{s,n}}\frac{\sin\left(\frac{\omega_{s,n}\tau}{2}\right)}{2\lambda_{s,n}h}J_1\left(k_{s,n}R\right)\cos\left[k_{s,n}r - \omega_{s,n}\left(t - \frac{\tau}{2}\right) - \frac{\pi}{4}\right]. \tag{4.19}$$

When $\mathcal{K}a \gg 1$ then (4.19) reduces to the free-surface solution, e.g. see Hendin & Stiassnie (2013), whereas when $\mathcal{K}a \ll 1$ the eigenvalues change fundamentally. The solution of Eq. (4.19) for a circular disturbance of $R = 15$ km with duration $\tau = 10$ s, residual displacement $\zeta_0 = 1$ m, $d = 20$ m and $h = 4$ km are shown in Fig. 7. The results are presented in term of bottom pressure time series for the first four AGW modes, at the distance of 1000 km from epicentre (*b*) and corresponding spectrum (*c*).

5. Mild Slope Equation for elastic ice sheet

Next we develop a mild slope equation (MSE) based on the eigenfunction structure for the problem with constant layer depths h. Similar to the ideas of MSE, presented in Kirby (1992) for incompressible fluid, the solution of a system of ice-water-bottom as waveguide is sought by wave equations in the water layer that satisfy the boundary conditions imposed by a possibly moving rigid sea bottom (i.e. earthquake) and the flexible ice plate. Employing the governing equation and boundary conditions described in §2, we derive a mild-slope model following a similar approach as described by Sammarco *et al.* (2013) and Abdolali *et al.* (2015). Using the separation, $\varPhi = f(z)\psi(x, y, t)$, we write the governing equation (2.1), which yields

$$\frac{1}{c^2}(f\psi)_{tt} - \nabla_r^2(f\psi) - f_{zz}\psi = 0. \tag{5.1}$$

Upon multiplication by f and integration over the depth, followed by using Leibniz's rule and boundary conditions at free surface and bottom, we neglect second-order terms in the substrate slope, staying within the classic mild-slope framework and obtain the MSE:

$$\left[\left(\frac{I_1^n}{c^2} + \frac{1}{g}\right)\psi_{n,t}\right]_{,t} - \nabla_r.(I_1^n \nabla_r \psi_n) + I_2^n \psi_n + \frac{1}{\rho g}\frac{\partial}{\partial t}(\delta P) - \frac{h_{n,t}}{\cosh(\lambda_n h)} = 0. \tag{5.2}$$

Substituting Eq. (2.5) in Eq. (5.2) yields

$$\begin{aligned}&\left[\left(\frac{I_1^n}{c^2} + \frac{1}{g}\right)\psi_{n,t}\right]_{,t} - \nabla_r.(I_1^n \nabla_r \psi_n) + I_2^n \psi_n \\ &\qquad + \nabla_r^2(\tilde{D}\nabla_r^2 \eta_t) + \nabla_r(\tilde{T}\nabla_r \eta_t) + \frac{\tilde{d}}{g}\eta_{ttt} - \frac{h_{n,t}}{\cosh(\lambda_n h)} = 0.\end{aligned} \tag{5.3}$$

Using kinematic boundary condition at surface, $\eta_t = f_z|_0 \psi_n = \lambda_n \tanh(\lambda_n h)\psi_n$ we obtain the final form of the hyperbolic MSE for weakly compressible fluid in arctic zones,

$$\begin{aligned}&\left[\left(\frac{I_1^n}{c^2} + \frac{1 + \tilde{d}\lambda_n \tanh(\lambda_n h)}{g}\right)\psi_{n,t}\right]_{,t} - \nabla_r.(I_1^n \nabla_r \psi_n) + I_2^n \psi_n \\ &+ \nabla_r^2\Big[\tilde{D}\nabla_r^2\Big(\lambda_n \tanh(\lambda_n h)\psi_n\Big)\Big] + \nabla_r\Big[\tilde{T}\nabla_r\Big(\lambda_n \tanh(\lambda_n h)\psi_n\Big)\Big] = \frac{h_{n,t}}{\cosh(\lambda_n h)},\end{aligned} \tag{5.4}$$

We allow slow variations in ice properties ($D(x)$ and $T(x)$). The model coefficients are

$$I_1^n = \int_{-h}^{0} f^2 dz = \frac{\sinh(2\lambda_n h) + 2\lambda_n h}{4\lambda_n \cosh^2(\lambda_n h)}; \qquad I_2^n = \int_{-h}^{0} f_z^2 dz = \lambda_n \frac{\sinh(2\lambda_n h) - 2\lambda_n h}{4\cosh^2(\lambda_n h)}. \tag{5.5}$$

It should be noted that the depth integrated models cannot consider sharp changes neither at ice properties nor bottom topography. It is due to mild slope variation of parameters and also due to the absence of higher order terms. Moreover, depth Integrated models cannot take into account the vertical variability of parameters like sound speed profile, which affect high frequency signals.

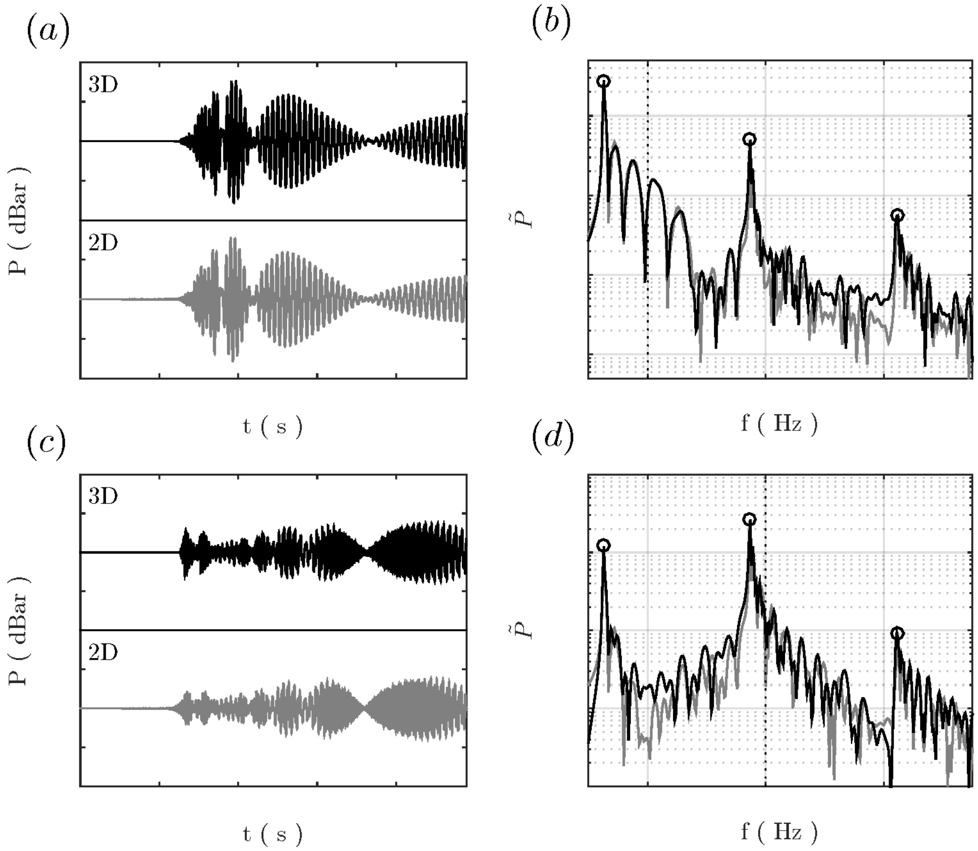

FIGURE 9. Bottom pressure time series (left panels) and corresponding spectra (right panels) according to the 3D (black) and depth-integrated (light grey) models at $X = 200$ km from source and in a constant depth, $h = 3000$ m, $d = 20$ m, The water and ice characteristics are the same as in Fig. 7. The unit source area with semi-length $b = 15$ km and $h_t = \sin(2\pi f_0 t)$ for rise time $\tau = 2/f_0$. (a,b) $f_0 = 0.2$ Hz and $\tau = 10$ s and (c,d) $f_0 = 0.4$ Hz and $\tau = 5$ s.

6. Model validation

Sample computations have been carried out to verify if the 2D model in the form of mild slope approximation (5.4) along with the analytical solution (4.19) can replace the 3D model concerning the direct numerical solution of (2.1). Note that the 3D model refers to the numerical solution of Equation (2.1) with boundary conditions defined by Eqs. (2.2) and (2.4). To start with, the analytical solution is compared to the 2D model for the first AGW mode at a distance of 90 km from the epicentre of a circular disturbance ($R = 15$) in a domain with 100 km radius. Although the analytical solution is based on an approximation for a relatively large distance (far-field), therefore, we have chosen 90 km from the epicentre to avoid lengthy numerical computations for 2D model. For the 2D model, frequency bands of width $\Delta f = 0.02$ Hz have been selected to discretise the forcing spectrum. The Sommerfeld radiation condition is applied at the outer open boundary, so that the waves leave the domain freely. To correctly reproduce the wavefield, for a given frequency the maximum mesh size is selected as $\Delta x = L/20$, where L is wave length. The time step is chosen according to Courant number $\leqslant 1$. The summation of model output for narrow frequency bands ($0.05 \leqslant f \leqslant 0.2$) is in good agreement in

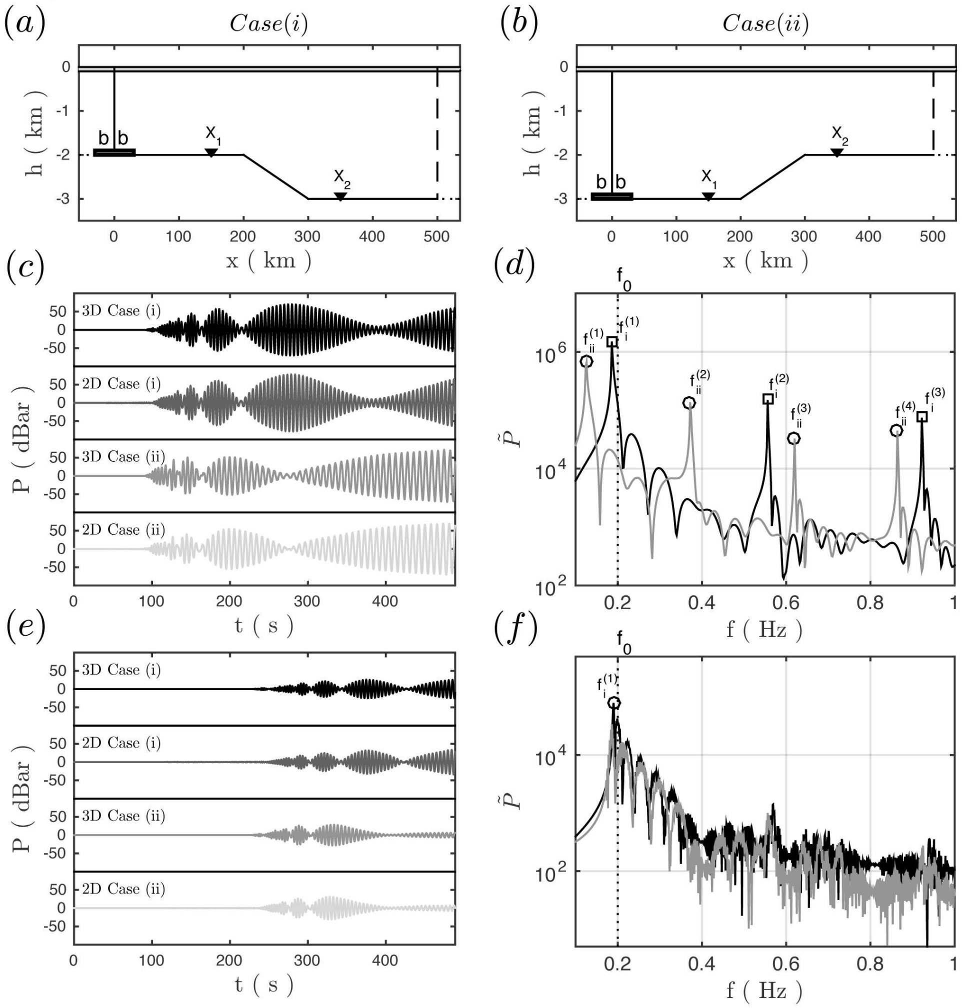

FIGURE 10. The case of varying sea bottom and constant ice sheet thickness with a tsunamigenic source at the shallower part (case *i*) and deeper part (case *ii*). (a,b) The computational domain. (c,e) Bottom pressure time series and (d,f) corresponding spectra at point X_1, 150 km, and point X_2, 350 km from the source. The unit source area with semi-length b=15 km, $d = 20$ m and $h_t = \sin(2\pi f_0 t)$ for rise time $\tau = 1/f_0 = 5$ s.

term of signal modulation, arrival time and peak frequency, $f^{(1)} = 0.093$ Hz, with the analytical solution for the first acoustic mode (Fig. 8).

In the second case, we validate the solutions for the case of constant depth $h = 3$ km and ice coverage $d = 20$ m. The domain consists of vertical section in $x; z$ through laterally uniform domains with no y-dependency. The source fault has semi-length of $b = 15$ km with maximum vertical displacement of $\zeta_0 = 1$ m. The numerical solvers are applied on a computational domain 500 km long; given the symmetry of the problem about the middle of the earthquake ($x = 0$), a fully reflective boundary condition is applied and computations are undertaken only for half of the physical domain. The computational time needed to reproduce 500 s of real-time simulation was approximately an order of magnitude less than for the 3D model. The results are presented for a virtual bottom gauge at $x = 200$ km in Fig. 9 in terms of the bottom pressure P and the corresponding

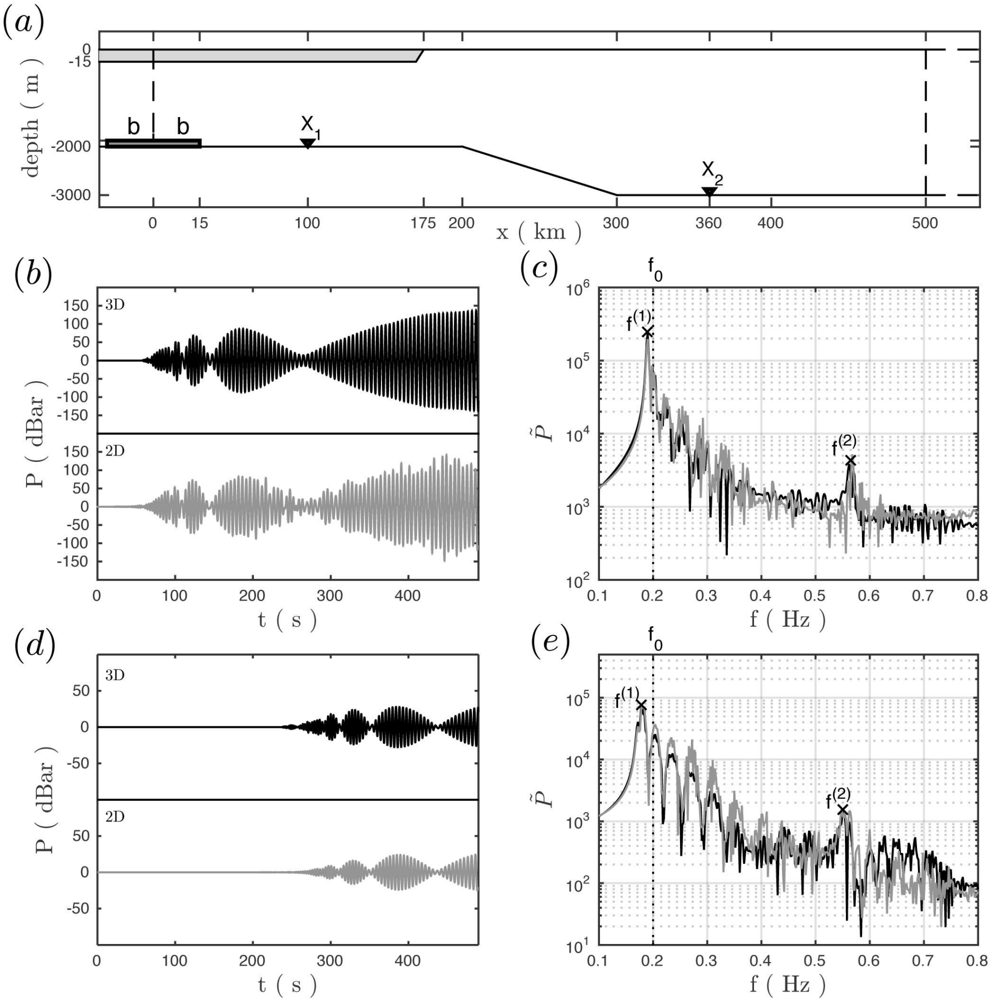

FIGURE 11. The case of varying sea bottom and partial ice sheet coverage over surface with a tsunamigenic source at the shallower part. (a) The computational domain. (b,c) Time series of bottom pressure time series and corresponding spectrum at point X_1, 100 km from the tsunamigenic source; and (d,e) point X_2, 360 km from the tsunamigenic source. The water and ice sheet characteristics are the same as in figure 2. The unit source area with semi-length b=15 km, $d = 15$ m and $h_t = \sin(2\pi f_0 t)$ for rise time $\tau = 1/f_0 = 5$ s.

spectrum $\tilde{P}$. In panels (a,b) the results relate to the case of $f_0 = 0.2$ Hz and $\tau = 10$ s and in panels (c,d) for the case of $f_0 = 0.4$ Hz and $\tau = 5$ s. The 3D model (black) and depth-integrated model (light grey) are in optimal agreement. The first three peak frequencies correspond to the cutoff frequency. The maximum number of AGW modes, N_{max}, is determined from (4.6) and (4.8), with $k_n = 0$ (corresponding to the cut-off frequency), so that

$$N_{max} = \begin{cases} \left\lfloor \omega h/c\pi + \frac{1}{2} \right\rfloor, & \mathcal{K}a \gg 1, \\ \\ \left\lfloor \omega h/c\pi + 1 \right\rfloor, & \mathcal{K}a \ll 1. \end{cases} \tag{6.1}$$

where the special brackets represent the floor function, i.e. largest integer from below. In the case $\mathcal{K}a \ll 1$ all progressive acoustic modes have to be considered in order to capture the whole spectrum properly, in particular upon transmission to shallower waters.

In the third case, a varying sea water depth with constant ice sheet thickness is considered in order to reveal AGW properties in deep and shallow water for the case of an earthquake in the shallower part of continental shelf (Case *i*) and in deeper part of computational domain (Case *ii*). In Fig. 10 the domain geometries are depicted in (a,b). The results are presented in term of bottom pressure at distance of X_1 =150 (c,d) and X_2 =350 km (e,f) from the moving sea bed. For case *i*, where water depth at generation zone is 2 km, the first three peak frequencies are approximately 0.187, 0.56 and 0.93 Hz, which can propagate toward points X_1 and X_2 as there is enough room in the wave guide. On the other hand and for case *ii*, the shallower part at right hand side of domain filters the first acoustic mode at source depth, therefore, the signals larger than 0.187 Hz can reach point X_2. The results from 3D and 2D solvers are in good agreement in term of amplitude, modulation and peak frequencies.

In the forth case, the domain is partially covered by a 175 km long ice sheet with $d = 15$ m thickness (Fig. 11). The rest of the numerical domain is imposed to barometric pressure ($d = 0$). The bed deformation, ice and water characteristics have the same values as previously. The bottom pressure time series are plotted at $X_1 = 100$ km in 2 km depth with ice sheet on the surface in panel (b,c) and at $X_2 = 360$ km in 3 km depth with free surface boundary. As is shown in Fig. 11, the formation of acoustic–gravity waves at source region is characterised by local depth and ice sheet properties, where both 3D (black) and 2D (light grey) models have similar time series and frequency spectrum.

7. Concluding remarks

We studied the effects of ice sheet on propagating acoustic–gravity waves (AGWs) in constant and varying water depths. To this end, we present an analytical model along with a numerical 2D depth-integrated and 3D models. The analytical model is only valid for constant depths, though it is computationally fast and accurate and can be employed for sensitivity analysis, as well as to estimate the source geometry. For large domains, the 3D model becomes computationally demanding, and thus a validation of the 2D model against the analytical solution was carried out. Note that the 2D model is in addition validated against the 3D model on a transect which resembles an infinite fault. The 2D model enables relatively fast calculations of real ocean floor geometry with partial ice coverage. It turns out that the dynamics of bed deformation vary the leading mode which is determined by N_{max} given by (6.1).

This work extends the capabilities of previous compressible models (Sammarco *et al.* 2013; Abdolali *et al.* 2015; Hendin & Stiassnie 2013) to include the effect of an elastic ice sheet on the sea surface following the ideas in Kirby (1992). Indeed, by expanding the capabilities of model equation, AGW field can be investigated in an integrated system of either bounded or free surface ocean.

Acknowledgments

J.T. Kirby acknowledges the support of the NSF Engineering for Natural Hazards program, grant CMMI-1537232.

REFERENCES

Abdolali, A & Kirby, J. T. 2017 Role of compressibility on tsunami propagation. *Journal of Geophysical Research: Oceans* (submitted).

Abdolali, A, Kirby, J. T. & Bellotti, G 2015 Depth-integrated equation for hydro-acoustic waves with bottom damping. *Journal of Fluid Mechanics* **766** (R1).

Caplan-Auerbach, J., Dziak, R. P., Bohnenstiehl, D. R., Chadwick, W. W. & Lau, T.-K. 2014 Hydroacoustic investigation of submarine landslides at west mata volcano, lau basin. *Geophysical Research Letters* **41** (16), 5927–5934, 2014GL060964.

Cecioni, C, Bellotti, G, Romano, A, Abdolali, A & Sammarco, P 2014 Tsunami early warning system based on real-time measurements of hydro-acoustic waves. *Procedia Engineering* **70** (C), 311–320.

Chierici, F, Pignagnoli, L & Embriaco, D 2010 Modeling of the hydroacoustic signal and tsunami wave generated by seafloor motion including a porous seabed. *Journal of Geophysical Research* **CO115**.

Eyov, E., Klar, A., Kadri, U. & Stiassnie, M. 2013 Progressive waves in a compressible-ocean with an elastic bottom. *Wave Motion* **50** (5), 929 – 939.

Hansen, J. 2007 Climate catastrophe. *New Scientist* **195** (2614), 30 – 34.

Hendin, G. & Stiassnie, M. 2013 Tsunami and acoustic-gravity waves in water of constant depth. *Physics of Fluids* **25** (8), 086103.

Hosking, RJ, Sneyd, Alfred David & Waugh, DW 1988 Viscoelastic response of a floating ice plate to a steadily moving load. *Journal of Fluid Mechanics* **196**, 409–430.

Kadri, U. 2014 Deep ocean water transport by acoustic-gravity waves. *Journal of Geophysical Research: Oceans* **119** (11), 7925–7930.

Kadri, U. 2015 Wave motion in a heavy compressible fluid: Revisited. *European Journal of Mechanics - B/Fluids* **49, Part A**, 50 – 57.

Kadri, U. 2016*a* Generation of hydroacoustic waves by an oscillating ice block in arctic zones. *Advances in Acoustics and Vibration* **2016** (ID 8076108), 1–7.

Kadri, U. 2016*b* Triad resonance between a surface-gravity wave and two high frequency hydro-acoustic waves. *European Journal of Mechanics - B/Fluids* **55, Part 1**, 157 – 161.

Kadri, U. 2017 Tsunami mitigation by resonant triad interaction with acoustic–gravity waves. *Heliyon* **3** (1), e00234.

Kadri, U. & Akylas, T. R. 2016 On resonant triad interactions of acoustic?gravity waves. *Journal of Fluid Mechanics* **788**.

Kadri, U. & Stiassnie, M. 2012 Acoustic-gravity waves interacting with the shelf break. *Journal of Geophysical Research: Oceans* **117** (C3), c03035.

Kadri, U. & Stiassnie, M. 2013 Generation of an acoustic-gravity wave by two gravity waves, and their subsequent mutual interaction. *Journal of Fluid Mechanics* **735**.

Kirby, J.T. 1992 Water waves in variable depth under continuous sea ice. *Proceedings of the Second International Conference on Offshore and Polar Engineering Conference* pp. 70 – 76.

Oliveira, T. C. A. & Kadri, U. 2016 Pressure field induced in the water column by acoustic-gravity waves generated from sea bottom motion. *Journal of Geophysical Research: Oceans* **121** (10), 7795–7803.

Renzi, E & Dias, F. 2014 Hydro-acoustic precursors of gravity waves generated by surface pressure disturbances localised in space and time. *Journal of Fluid Mechanics* **754**, 250–262.

Sammarco, P, Cecioni, C, Bellotti, G & Abdolali, A 2013 Depth-integrated equation for large-scale modelling of low-frequency hydroacoustic waves. *Journal of Fluid Mechanics* **722**, R6.

Schulkes, R.M.S.M., Hosking, R.J. & Sneyd, A.D. 1987 Waves due to a steadily moving source on a floating ice plate. part 2. *Journal of Fluid Mechanics* **180**, 297?318.

Stiassnie, M 2010 Tsunamis and acoustic-gravity waves from underwater earthquakes. *Journal of Engineering Mathematics* **67** (1-2), 23–32.

Yamamoto, Tokuo 1982 Gravity waves and acoustic waves generated by submarine earthquakes. *International Journal of Soil Dynamics and Earthquake Engineering* **1** (2), 75 – 82.

Zakharov, D.D. 2008 Orthogonality of 3d guided waves in viscoelastic laminates and far field evaluation to a local acoustic source. *International Journal of Solids and Structures* **45** (6), 1788 – 1803.